Complex Structure of Molten FLiBe (2LiF–BeF_2) Examined by Experimental Neutron Scattering, X-Ray Scattering, and Deep-Neural-Network Based Molecular Dynamics

Sean Fayfar,[1] Rajni Chahal,[2] Haley Williams,[3] D. Nathanael Gardner,[3] Guiqiu Zheng,[1] David Sprouster,[4,1] Jörg C. Neuefeind,[5] Dan Olds,[6] Andrea Hwang,[7] Joanna Mcfarlane,[8] Ryan C. Gallagher,[8] Mark Asta,[7] Stephen Lam,[2,‡] Raluca O. Scarlat,[3,†] and Boris Khaykovich[1,*]

[1] *Nuclear Reactor Laboratory, Massachusetts Institute of Technology, Cambridge, Massachusetts 02139, USA*
[2] *Department of Chemical Engineering, University of Massachusetts Lowell, Lowell, Massachusetts 01854, USA*
[3] *Department of Nuclear Engineering, University of California, Berkeley, California 94720, USA*
[4] *Department of Materials Science and Chemical Engineering, Stony Brook University, Stony Brook, New York 11784, USA*
[5] *Neutron Sciences Directorate, Oak Ridge National Laboratory, Oak Ridge, Tennessee 37831-6475, USA*
[6] *National Synchrotron Light Source II, Brookhaven National Laboratory, Upton, New York 11973, USA*
[7] *Department of Materials Science and Engineering, University of California, Berkeley, California 94720, USA*
[8] *Fusion and Fission Energy and Science Directorate, Oak Ridge National Laboratory, Oak Ridge, Tennessee 37831-6475, USA*

(Received 15 August 2023; revised 10 November 2023; accepted 29 November 2023; published 5 January 2024)

The use of molten salts as coolants, fuels, and tritium breeding blankets in the next generation of fission and fusion nuclear reactors benefits from furthering the characterization of the molecular structure of molten halide salts, paving the way to predictive capability of the chemical and thermophysical properties of molten salts. Due to its neutronic, chemical, and thermochemical properties, 2LiF-BeF_2 is a candidate molten salt for several fusion- and fission-reactor designs. We performed neutron and x-ray total-scattering measurements to determine the atomic structure of liquid 2LiF-BeF_2. We also performed *ab initio* and neural-network molecular-dynamics simulations to predict the structure obtained by neutron- and x-ray-diffraction experiments. The use of machine learning provides improvements to the efficiency in predicting the structure at a longer length scales than is achievable with *ab initio* simulations at significantly lower computational expense while retaining near *ab initio* accuracy. We found that the NNMD simulations accurately predicted the BeF_4^{2-} oligomer formations seen in the experimental first-structure-factor peak. Our combination of high-resolution measurements with large-scale molecular dynamics provided an avenue to explore and experimentally verify the intermediate-range ordering beyond the first-nearest neighbor that has posed too many experimental and computational challenges in previous works. With a deeper understanding of the salt structure and ion ordering, the evolution of salt chemistry over the lifetime of a reactor can be better predicted, which is crucial to the licensing and operation of advanced fission and fusion reactors that employ molten salts. To this end, this work will serve as a reference for future studies of salt structure and macroscopic properties with and without the addition of solutes.

DOI: 10.1103/PRXEnergy.3.013001

I. INTRODUCTION

Molten salts have garnered a resurgence of interest due to their favorable use in energy applications such as advanced next-generation nuclear power plants [1–3]. These include fluid-fueled molten-salt reactors (MSRs) that employ fluoride or chloride salts [4,5], solid-fueled reactors that employ salt as a high-temperature coolant, such as the fluoride-salt-cooled high temperature reactor (FHR) [6], and fusion reactors such as the affordable robust compact (ARC) reactor, which uses 2LiF-BeF_2 as both a coolant and a tritium breeding blanket [7,8]. Molten salts provide high volumetric heat capacity and a wide range of thermal stability that allow reactors to deliver a larger fraction of their heat at higher temperatures compared with traditional designs. This increase in heat-to-electricity efficiency, along with the

*bkh@mit.edu
†scarlat@berkeley.edu
‡Stephen_Lam@uml.edu

possibility of diverse energy products at higher temperatures, enhances the economic competitiveness of salt-based nuclear-energy systems [9,10]. Additionally, the ability to operate at nearly atmospheric pressure enables the design of passive safety systems and inherent safety features that help meet high safety standards with greater simplicity of design and, consequently, with potentially lower development costs and shorter development time lines [11,12].

A number of salt compositions are candidates for use in MSRs, with FLiBe (2LiF-BeF_2) being the focus of this study [13–17]. Experimentally determining the thermochemical and thermophysical properties, such as the density, viscosity, thermal expansion, specific heat, and others, has been the focus of a number of studies [18–26]. Electroanalytical studies have sought to characterize ionic transport as well as the liquidus in LiF-BeF_2 systems [27–29]. Additional studies have focused on measuring the atomic structure of molten-salt candidates [30–33] and their corrosive effects on structural materials [34–39]. With the vast possibilities of salt compositions, predictive modeling can alleviate experimental bottlenecks associated with characterizing new salt mixtures [40–42]. To successfully ascertain the physical characteristics of molten salts using simulations, their atomic structure needs to be measured experimentally to validate the assumptions required in simulations. Furthermore, an understanding of salt structure provides the basis for understanding the macroscopic thermochemical and thermophysical properties of a salt and, thus, may provide an avenue for better predicting the evolution of salt within a reactor with changes in temperature and composition. The relationship between the structure of a molten salt and its conductivity and/or ion transport, viscosity, and solvation behavior has been analyzed in several studies [43–45]. Broadly, salt structure has been characterized by its solvoacidity, or its degree of association or dissociation as measured by the chemical activity of its Lewis base—F^- in the case of fluoride salts [46–48]. Salt chemistry and fluoroacidity encompass both composition and structure: i.e., what ions are present and how they interact. By characterizing the interactions among ions in a melt, we gain access to a more fundamental understanding and a greater predictability of salt behavior.

The structure of molten LiF-BeF_2 solutions was studied by x-ray diffraction (XRD) 50 years ago by Vaslow and Narten [49], using a MoK_α laboratory x-ray source. They verified tetrahedral geometry for BeF_4^{2-} complex ions as in the model developed by Baes [50] and output nearest-neighbor (NN) distances and coordination numbers (CN) for Be—F, Li—F, and F—F. They postulated corner-sharing tetrahedra, showing a consistent Be—F CN of 4 for binary melts across the entire composition space from 100% LiF to 100% BeF_2. This postulation was further supported by molecular-dynamics models that predicted NN and CN for $LiBeF_3$; the Be—F values were within two standard deviations, the F—F values were identical between molecular-dynamics (MD) predictions and experiments, and the Li—F NN distance predicted by MD at 760 °C was more than three standard deviations smaller than x-ray–measured values at 400 °C [51].

Evidence of tetrahedral BeF_4^{2-} in molten LiF-BeF_2 solutions is ubiquitous, beginning with measurements using XRD and vibrational spectroscopy (infrared and Raman) along with molecular-dynamics studies [49,51–53]. Evidence of dimers and higher-order oligomers increasing with the BeF_2 concentration has followed from Raman spectroscopy and thermodynamic models fitted to measured activity coefficients and other thermochemical data [42,54–56]. The formation of corner-sharing tetrahedral BeF_4^{2-} clusters (which was proposed from considering fluoroberyllate melts as analogous to SiO_4 melts) [50] has been reinforced by modern molecular-dynamics simulations [40,42,44,57,58]. However, the ability to validate the intermediate-range melt structure predicted in molecular simulations is limited by the resolution of experimental XRD data available in the literature [49]. With the NN structure of fluoroberyllate melts described and validated, it now becomes possible to investigate the role of intermediate-range order on solvation mechanisms and other macroscopic physical and chemical properties of fluids. Thus, validating molecular-dynamics models for their structure predictions beyond the NN would be highly impactful.

Molecular-dynamics simulations have revolutionized the ability of researchers to discover and assess new materials, aiding interpretation, error analysis, sensitivity analysis, and prioritization of experimental studies. *Ab initio* molecular-dynamics simulations (AIMDs) have been the premier method for modeling molten-salt structure and predicting physical properties [41]. However, due to high computational costs, AIMD simulations are practically limited to small system sizes (fewer than hundreds of atoms). Meanwhile, classical interatomic potentials can simulate large system sizes but have recently been shown to inaccurately predict relative populations of bond angles and clusters, which play an important role in determining the thermophysical and thermochemical behavior in structurally complex salt mixtures [59]. While such simulations have been used to interpret the general features and structures that exist in an experimental x-ray or Raman spectrum, precise reconstruction and detailed analysis has not been possible. To overcome these limitations, recent developments of neural-network molecular-dynamics simulations (NNMDs) have demonstrated that NNMD simulations can achieve near *ab initio* accuracy, at orders-of-magnitude-higher speed and scalability, for predicting the structures and properties of molten salts [60–64]. Moreover, it has recently been shown that larger NNMD simulations were required for

accurately capturing the intermediate-range structures beyond the first solvation shell that can emerge in salts containing significant fractions of multivalent cations such as Zr [59]. Structures of similar length scale have also been predicted for LiF-BeF_2 with dissolved tritium [45,65].

In this work, we present a structural characterization of molten FLiBe including total-scattering measurements and molecular-dynamics simulations. We examined FLiBe using both neutron and XRD from room temperature up to 700 °C, well above the melting point and in the typical range for energy applications including advanced fission and fusion reactors. Our measurements, conducted using renowned sychrotron–x-ray and spallation-neutron facilities, enabled higher resolution than prior XRD measurements and a degree of detail inaccessible to previous studies. The use of both x-ray and neutron-scattering techniques allows for insight into each species (Li, Be, F), given their differing x-ray atomic form factors and neutron-scattering lengths. These high-resolution measurements are necessary to validate new molecular-dynamics techniques and investigate the intermediate-range ordering present within FLiBe. We performed AIMD and NNMD simulations to interpret the structural peaks found in measurements and we provide several validation experimental data sets for both short-range and intermediate-range order in FLiBe melts at multiple temperatures. Our neutron total-scattering measurements provide new evidence for the intermediate-range structure seen in the first diffraction peak that is necessary to validate emerging molecular-dynamics models.

II. EXPERIMENTAL AND COMPUTATIONAL METHODS

A. Sample preparation

A 2:1 stoichiometric ratio of LiF and BeF_2 was prepared with isotopically enriched ^{7}LiF provided by Oak Ridge National Laboratory (ORNL) and BeF_2 from Materion. To prepare the sample for neutron-scattering measurements, a 1.3(1)-g sample of FLiBe was placed and melted in a vanadium canister and sealed with a flanged titanium lid and a graphite-foil gasket. FLiBe has a melting point of 459.1(2) °C [23,29]. The sealed canister was subsequently cleaned from beryllium contamination by thoroughly wiping the canister with Ghost Wipes and then sampling with a Ghost Wipe to ensure that the surface contamination was below the free-release limit of 0.2 μg Be per 100 cm^2. For x-ray scattering measurements, a sample of FLiBe (prepared from constituent Materion salts) was loaded and melted into a capped graphite insert and then placed into a flame-sealed quartz NMR tube [33].

The ^{7}Li-enriched sample used in this study was believed to be of approximately 99% enrichment, though the stock ^{7}LiF was a legacy sample from ORNL and was not labeled with a numerical value. We include a comparison between a 99% and 95% ^{7}Li-enriched sample in Fig. S4 of the Supplemental Material [66] by weighting the NNMD results.

B. Neutron and x-ray scattering

Neutron total-scattering measurements were performed at the NOMAD beamline [67] at the Spallation Neutron Source (SNS). Samples were loaded into vanadium sample cans and placed into the vanadium furnace to measure the sample from room temperature up to 700 °C. The sample was heated using the vanadium furnace provided at the beamline; the sample was measured upon heating, with an exposure time of 5 min for each measurement. Once the sample had reached 550 °C and 700 °C, the sample was measured for 7.6 h at each temperature. The measurements at the beamline were calibrated using standard samples such as diamond and vanadium. The measurements were background corrected by subtracting the empty sample container [67]. The raw neutron-scattering intensity was converted to the total (static) structure factor $S(Q)$ with corrections using the ADDIE software package [68] at the beamline (shown in Figs. S5 and S6 of the Supplemental Material [66]). Q is the scattering vector and is defined as $Q = 4\pi/(\lambda)\sin\theta$ for elastic scattering, where λ is the wavelength of the radiation and 2θ is the diffraction angle. NOMAD has a Q range that extends out to 150 $Å^{-1}$. However, the Q_{max} used was 50 $Å^{-1}$ for the structure factor and the Fourier analysis before filtering (discussed in the Supplemental Material [66]).

XRD measurements were conducted at the pair-distribution-function (PDF) beamline (28-ID-1) [69] at the National Synchrotron Light Source II (NSLS-II). The sample was placed in a novel sample holder designed to contain molten salts that includes a sealed quartz capillary with a capped graphite insert to hold the salt [33]. The x-ray measurements were performed with an amorphous-silicon-based flat-panel detector mounted orthogonal to the beam path that moved between two distances for PDF and XRD measurements [69]. At the high-Q PDF distance, the instrument measures a Q value out to 33 $Å^{-1}$, and we used a Q_{max} of 20 $Å^{-1}$ for Fourier analysis. The distance was calibrated by measuring a LaB_6 standard sample. The sample was heated using a hot-air blower at a rate of 5 °C per minute until it reached 510 °C. The sample was measured while heating with an exposure time of 30 s for each measurement. Once at 510 °C, the sample was measured with an exposure time of approximately 5 min. The raw two-dimensional detector images were corrected using standard procedures such as subtracting the detector dark current and masking regions with artifacts. The corrected images were radially integrated and converted into the scattering intensity as a function of the scattering vector Q [70]. Patterns of the empty graphite quartz container were also

measured and were subtracted from the sample measurements (see Figs S7 and S8 of the Supplemental Material [66]). The x-ray scattering intensities were converted into the total structure factor $S(Q)$ using the PDFgetX3 software package [71], which uses an *ad hoc* data-correction method to obtain the coherent x-ray scattering intensities. The sample temperature was calculated using the methods described by Sprouster *et al.* [33].

The total structure factor $S(Q)$ calculated from the total-scattering intensity is composed of partial structure factors dependent on the salt components through

$$S^{(\mathrm{n/x})}(Q) = \sum_{\alpha,\beta\geq\alpha} S_{\alpha\beta}^{(\mathrm{n/x})}(Q) = \sum_{\alpha,\beta\geq\alpha} w_{\alpha\beta}^{(\mathrm{n/x})}(Q) S_{\alpha\beta}(Q), \quad (1)$$

with

$$w_{\alpha\beta}^{(\mathrm{n/x})}(Q) = \frac{c_\alpha c_\beta f_\alpha(Q) f_\beta(Q)}{\left[\sum_\alpha c_\alpha f_\alpha(Q)\right]^2}\left(2-\delta_{\alpha\beta}\right), \quad (2)$$

where α and β are coefficients representing the salt components, c is the concentration of the atomic species, $f(Q)$ is the x-ray form factor [72], and $\delta_{\alpha\beta}$ is the Kronecker delta function. The weights $w_{\alpha\beta}$ are normalized such that they sum to one for all values of Q. For neutron scattering, the x-ray atomic form factors are replaced with the neutron-scattering lengths b, which are independent of Q. The superscripts indicate that the structure factor or PDF was weighted using Eq. (2) for neutrons (n) or x rays (x). A discrete Fourier sine transform is used to calculate the PDF $g(r)$, as

$$g(r) - 1 = \frac{1}{2\pi^2\rho_0}\sum_{Q}^{Q_{\max}} Q\left[S(Q)-1\right]\frac{\sin Qr}{r}\Delta Q, \quad (3)$$

where ρ_0 is the average number density and r is the distance from a reference atom. The inverse Fourier sine transform calculates the structure factor from the PDF:

$$S(Q) - 1 = 4\pi\rho_0 \sum_{r}^{r_{\max}} r\left[g(r)-1\right]\frac{\sin Qr}{Q}\Delta r. \quad (4)$$

The PDF is the ratio of the atomic density at a distance r from a central atom to the bulk density [73–76]. Note that the unweighted partial PDF $g_{\alpha\beta}$ that we discuss is also commonly referred to as the radial distribution function (RDF) [40,44,62,65].

C. Coordination-number calculations

The coordination numbers (CN), $N(r)$, were calculated by integrating the area under the partial PDF using

$$N(r_{\min}) = 4\pi\rho_\beta\int_0^{r_{\min}} r^2 g_{\alpha\beta}(r)dr = \frac{4\pi\rho_\beta}{w_{\alpha\beta}^{(\mathrm{n/x})}}\int_0^{r_{\min}} r^2 g_{\alpha\beta}^{(\mathrm{n/x})}(r)dr, \quad (5)$$

where $\rho_\beta = c_\beta\rho_0$ is the number density of the β atoms around a central α atom [40,75,77]. The $r_{\min}$ value is chosen as the first minimum in the partial PDFs.

The first-peak locations were determined by fitting the simulated partial PDFs with a skewed Gaussian and calculating the location of the maximum. The error estimate comes from the fitting procedure. To find the first-peak locations for the neutron and x-ray measurements, we fitted our results with three skewed Gaussians summed together. The peak location was calculated by finding the maximum point on the component Gaussians. The experimental coordination numbers were calculated by integrating the component Gaussian and removing the weight factor as shown in Eq. (5) [78–80] (for more details, see Figs. S10 and S11 of the Supplemental Material [66]). Determination of the x-ray coordination numbers was not feasible using this method, because the weight factor $w_{\alpha\beta}$ depends on Q.

We note also that the coordination numbers depend on the chosen cutoff value, $r_{\min}$, at the first minimum $g_{\alpha\beta}(r)$, as shown in Eq. (5). The Be—F partial PDF has a clear minimum at zero and we use a $r_{\min}$ value of 2.35 Å. However, Winner *et al.* [44] have argued that $r_{\min}$ (referred to as the first-coordination-shell radius) for F—Be should be 1.92 Å, which resulted in their CN result of 3.9. Using a $r_{\min}$ value of 1.92 Å with our NNMD partials at 700 °C, we find the CN to be 3.89, which matches their results more closely.

D. Molecular-dynamics simulations

1. Ab initio molecular-dynamics simulations

A supercell containing 91 atoms was used (13 Be, 26 Li, and 52 F). The simulation-cell volume was imposed based on the FLiBe density of 2.0314 g/ml and 1.937 g/ml at 510 °C and 700 °C, respectively [81]. More recent experiments have found the density of FLiBe to be 2.029(11) g/ml and 1.948(14) g/ml at 510 °C and 700 °C, respectively, with a molecular weight of 33.02(5) g/mol, an LiF/BeF_2 molar ratio of 1.977, and 93.12% ^{7}Li enrichment [23]. Assuming natural isotopics for ^{7}Li of 92.5% and 6.94 g/mol Li atomic weight, the cell lengths are 10.17 Å and 10.33 Å, respectively. The AIMD simulations were performed under Born-Oppenheimer approximations using the Vienna *ab initio* simulation package (VASP) [82]. For electronic self-consistent calculations, the

generalized-gradient approximation (GGA) in the form of the Perdew-Burke-Ernzerhof (PBE) exchange correlation functional was adopted [83]. The following projector augmented wave (PAW) pseudopotentials provided by VASP were used to model the core electrons in FLiBe: Be ($2s^2$), Li_sv ($1s^2\ 2s^1$), and F ($2s^2\ 2p^5$). There was a large plane-wave cutoff of 600 eV with a 1×10^{-5} eV convergence criterion for electronic self-consistent steps. The calculations were performed using a single (gamma) k point. The parameters chosen yield convergence with 2 meV per atom. To account for the effect of dispersion interactions, the density-functional-theory (DFT)-D3 formulation proposed by Grimme *et al.* [84] was used. This formulation has previously been found to most closely match the experimental density for the FLiBe system. All calculations were performed allowing for spin polarization. The canonical (NVT) ensemble using a Nosé-Hoover thermostat [85] was employed while maintaining periodic boundary conditions. The supercell was first initialized with a random structure generated with the PACKMOL software package [86] to avoid overlapping atomic positions. The initial random configuration was equilibrated at 510 °C and 700 °C for 20 ps to develop the liquid structure. Once equilibrated, the nearly 50-ps simulation trajectory should be sufficient to obtain a converged molten-salt structure and properties according to our previous work [87]. A time step of 2 fs was used for all of the AIMD simulations. The pressure of the equilibrated fixed-volume cells was −500 and −300 MPa, respectively (95% confidence interval).

2. NNIP training

For training of the neural-network interatomic potential (NNIP), the DeePMD-kit (DP-kit) software package (version 1.3.3) was employed [88]. The Deep-Pot-Smooth Edition (DeepPot-SE) potential contained inside the DP-kit was chosen due to a smooth and continuously differentiable potential-energy-surface generation [89]. The DeepPot-SE model learns a mapping between the local environment of each atom within an 8-Å cutoff to a per-atom energy, such that the sum of the atomic energies corresponds to the reference DFT energy. The gradients of the NNIP predicted energies are then used to compute the atomic forces. Both the reference energies and forces are included to evaluate the loss function, which is minimized during training of a DeepPot-SE model. The training data set comprised 11 019 configurations at 510 °C and 10 283 configurations at 700 °C, containing LiF and BeF_2 of the AIMD simulations with 91-atom supercells. During the training, the data sets were shuffled and were split into 80% and 20% for training and validation, respectively. Here, a smooth-cutoff and hard-cutoff radius of 2 Å and 8 Å, respectively, were chosen. The inclusion of a smooth-cutoff radius in the DeePMD-SE model avoids sudden discontinuity when evaluating atomic forces by introducing a weighting function that smoothly degrades to zero between the smooth- and hard-cutoff radius. The atomic environment within the hard-cutoff radius of 8 Å is considered to evaluate the atomic centric descriptor, which is eventually mapped to the atomic energies during model training (for additional details, see the Supplemental Material [66]). The embedding-network and fitting-network size were {25,50,100} and {240,240,240}, respectively. The tunable prefactors in the loss function were chosen at 0.002, 1000, 1, and 1 for p_e^{start}, p_f^{start}, p_e^{limit}, and p_f^{limit}, respectively. These network parameters have previously resulted in well-fitted potential-energy surfaces for multi-component molten-salt systems [59,62]. Here, the network was only trained on AIMD energies and forces. The trained network using DeepPot-SE yielded energy and force errors of 1.92 meV per atom and 22.1 meV/Å, respectively, for the validation set. The resulting errors are within the precision of DFT. The low energy and force-training testing errors suggest a well-fitted potential-energy surface.

3. Neural-network molecular dynamics using developed NNIP

The trained NNIP potentials were used in the Large-Scale Atomic/Molecular Massively Parallel Simulator (LAMMPS) molecular-dynamics program via the interface with DeePMD-kit [90]. The NNIP-based molecular-dynamics (NNMD) simulations allow for simulating the larger simulation-cell parameters that are required to gain sufficient resolution at $Q \sim 1$ Å^{-1}. For this purpose, cell parameters of 20.33 Å and 20.66 Å were chosen for the NNMD simulations of FLiBe at 510 °C and 700 °C, respectively, comprising 728 atoms (208 Li, 104 Be, and 416 F) and corresponding to liquid densities of 2.0314 g/ml and 1.937 g/ml, respectively. During the NNMD simulations, at least 2 ns simulations were performed using 2-fs time steps and employing the Nosé-Hoover thermostat [91] in a constant-volume ensemble (NVT). Periodic boundary conditions were maintained in all three directions. After 0.5 ns of equilibration, trajectories longer than 1.5 ns were used to study radial distribution functions as well as to perform structure-factor calculations. More details on the analysis are provided in the following sections.

E. Quantifying agreement between experiments and simulations

To evaluate the agreement between the simulations and the experimental results, we calculated the R_χ factor proposed by Wright [92] and used by others [93–96], which is defined by

$$R_\chi = \left(\sum_i \left[f_{exp}(x_i) - f_{sim}(x_i) \right]^2 / \sum_i f_{exp}^2(x_i) \right)^{1/2}. \quad (6)$$

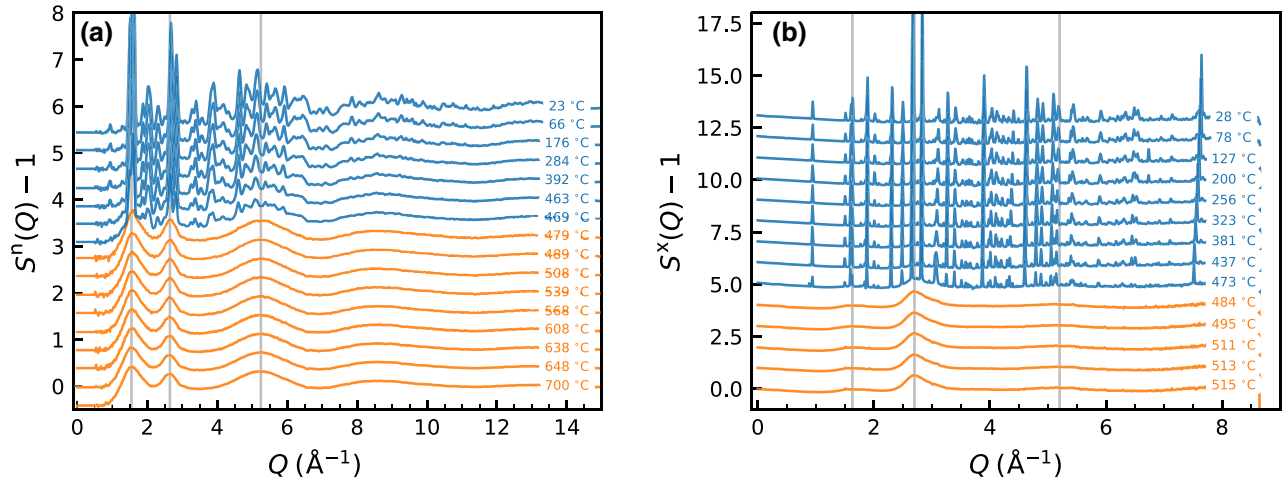

FIG. 1. The total (a) neutron and (b) x-ray structure factors of FLiBe at various temperatures above (orange) and below (blue) the melting point.

Here, f_{exp} and f_{sim} correspond to measured and simulated $S(Q)$ and $g(r)$. All of the R factors are calculated and listed in Table S1 of the Supplemental Material [66]. We evaluated the structure factor in the range $1 \leq Q \leq 15$ Å^{-1} and the PDF in the range $1 \leq r \leq 10$ Å, except for the AIMD results, which extend to only approximately 5 Å. All of these values are presented in Table S1 of the Supplemental Material [66].

III. RESULTS

The results of the total structure-factor measurements using neutrons and x rays while heating above and below the melting point of FLiBe are displayed in Fig. 1. At the lower temperatures, the crystalline Bragg peaks are clearly visible until the sample fully melts around 470 °C. At temperatures above the melting point, a few peaks remain, broader and of lower intensity than for the solid phase, and most of the higher-Q peaks are no longer present. Once molten, the liquid peaks only have small changes upon further heating, with the peak intensity decreasing and moving toward smaller Q values (see Fig. S12 of the Supplemental Material [66]). The partial PDFs and partial structure factors predicted by the NNMD simulations at 700 °C are shown in Fig. 2 for each of the atomic pairs in FLiBe; the same results from our AIMD simulations, and from prior studies by Winner *et al.* [44] and Attarian *et al.* [58], all showing similar features, are provided in Figs. S2 and S3 of the Supplemental Material [66].

Our x-ray scattering measurements of molten FLiBe are compared to those measured by Vaslow and Narten [49] and displayed in Fig. 3. We find the small first peak in the reduced structure factor at 1.7 Å^{-1}, which Vaslow and Narten [49] observed to increase with the concentration of BeF_2 in LiF-BeF_2 mixtures. The first three peaks in the reduced structure factor match closely in position but vary slightly in intensity, likely due to changes in data processing. Our measurements have much higher

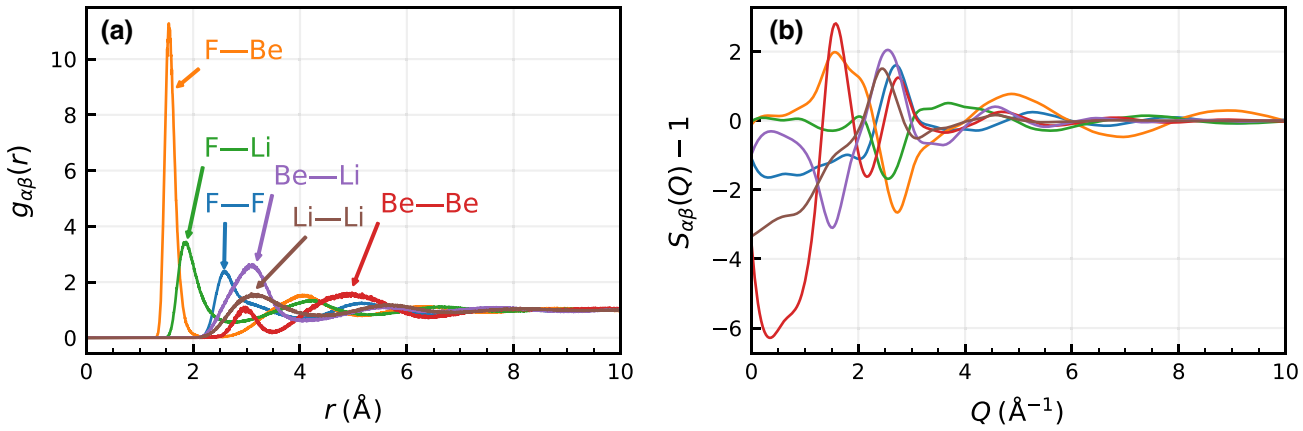

FIG. 2. The NNMD simulation results of the (a) unweighted partial PDFs and (b) unweighted partial structure factors of FLiBe at 700 °C.

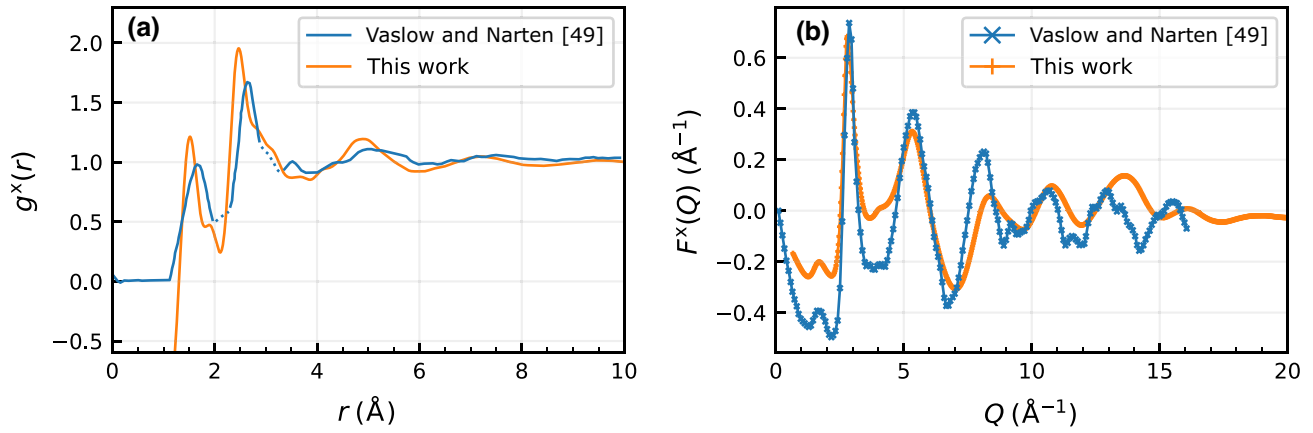

FIG. 3. The x-ray (a) PDF and (b) reduced structure function from this study (at 510 °C) and from Vaslow and Narten [49] (at 555 °C). Note that the reduced structure function is defined as $F(Q) = Q[S(Q) - 1]$. The dashed portions of the Vaslow PDF results were reported as artifacts resulting from the limited Q range.

resolution and extend out further in Q, which improves the quality of real-space PDF measurements. Our PDF measurements contain the same two large peaks at 1.5 Å and 2.5 Å, with slight differences in position and intensity. Additionally, we resolve the small peak at 1.9 Å that was displayed with dashed lines and attributed as an artifact from their limited Q range.

The results of the total structure factor of FLiBe at 550 °C and 700 °C from neutron measurements are included in Fig. 4, compared with corresponding neutron-weighted results from AIMD and NNMD simulations. The experimental structure-factor measurements were used to calculate the PDF [using Eq. (3)] for real-space analysis to compare with the simulated PDFs. These partial PDFs reveal the atomic pairs that produce the peaks measured with experiments, such as the main peak at 1.56 Å, being the result of Be—F correlations. The NN peak locations and CNs are included in Table I. We found the neutron and

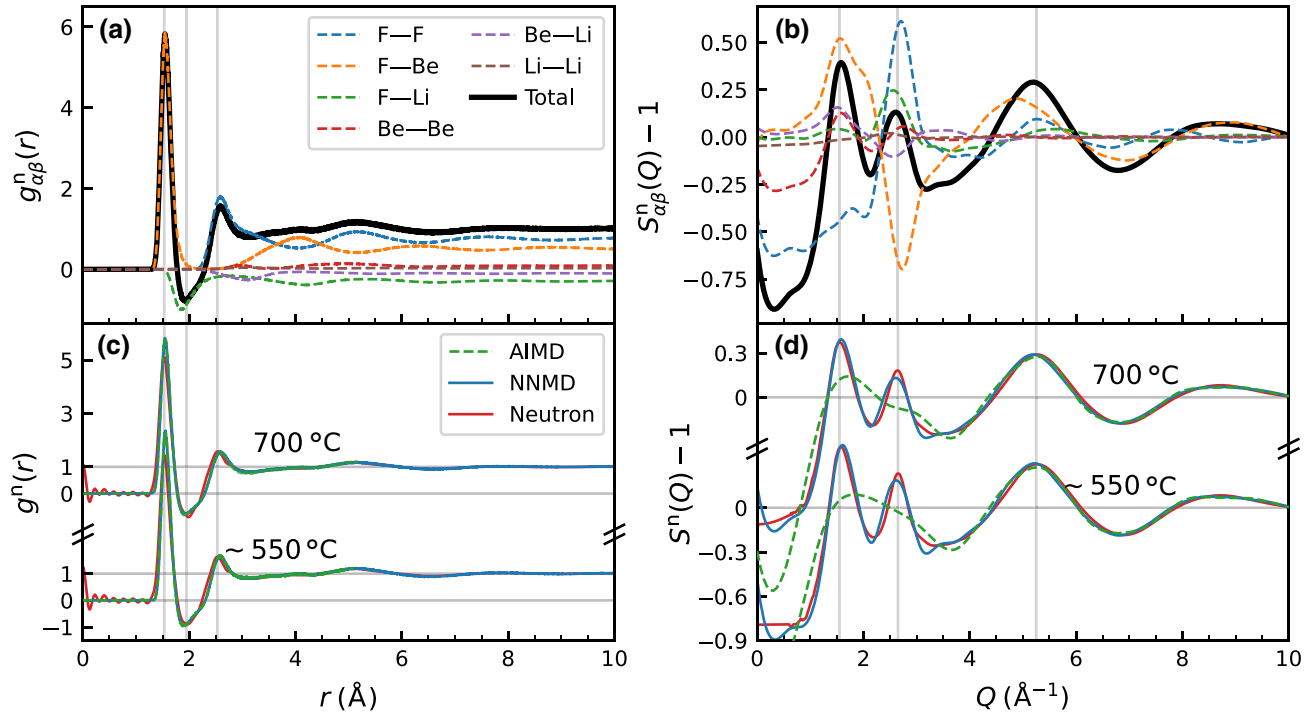

FIG. 4. The experimental and computational results of the neutron PDF and structure factor of FLiBe at 550 °C and 700 °C. (a),(b) The NNMD simulation results weighted with neutron-scattering lengths. (c),(d) The neutron-scattering results with AIMD and NNMD simulation results for comparison. Note that the MD results are at 510 °C.

TABLE I. The experimental and computational results of the first-peak locations and coordination numbers of FLiBe. CNs from AIMD and NNMD were calculated by integrating the partial $g_{\alpha\beta}(r)$ using Eq. (5).

	Temperature	Nearest-neighbor distance (Å)				$r_{\min}$	Coordination number		
Pair	(°C)	AIMD	NNMD	Neutron	X ray	(Å)	AIMD	NNMD	Neutron
F—Be	700	1.548(1)	1.546(1)	1.53(1)	···		3.99(5)	3.97(5)	3.67(15)[a]
	550	···	···	1.53(1)	···	2.35	···	···	3.73(15)[a]
	510	1.552(1)	1.551(1)	···	1.51(1)		4.00(5)	4.00(5)	···
F—Li	700	1.850(2)	1.849(3)	1.95(2)	···		4.52(8)	4.50(8)	···
	550	···	···	1.92(2)	···	2.75	···	···	···
	510	1.854(2)	1.860(2)	···	1.92(2)		4.63(8)	4.66(8)	···
F—F	700	2.585(5)	2.587(6)	2.53(1)	···		···	···	···
	550	···	···	2.52(1)	···		···	···	···
	510	2.576(4)	2.579(5)	···	2.47(1)		···	···	···

[a]Because neutron-diffraction measurements only provide total $g^n(r)$, the CNs were determined by integrating Gaussians fitted to the total $g^n(r)$; we observe the uncertainty introduced by this method to be ±0.15.

x-ray Be—F and F—F experimental NN distances to be smaller than those found through simulations and Li—F had larger distances.

The results of the structure factor from XRD measurements are presented in Fig. 5 with the same AIMD and NNMD simulation results weighted using x-ray atomic form factors. These partial $S^{x}_{\alpha\beta}$ reveal the atomic correlations producing the scattering peaks, such as the first peak at 1.7 $Å^{-1}$, being comprised of Be—F and F—F, which Vaslow and Narten [49] found to increase with the BeF_2 concentration. The first peak measured with x rays around 1.7 $Å^{-1}$ is significantly weaker than the neutron-scattering measurements because the atomic form factor for fluorine is 5 times larger than for the other two atoms in FLiBe. This causes a much lower peak than measured with neutrons and is evident with the NNMD x-ray weighted results in Fig. 5(b). From the same reasoning, the second peak at 2.7 $Å^{-1}$ is dominant in the x-ray measurements. The peak position and intensity in the simulated structure factors match closely with the experimental results [Fig. 5(d)]. The small first peak matches better in position and intensity between the NNMD simulations and the x-ray scattering measurements than the second peak, which is predicted from the NNMD simulations to be at a slightly lower Q value and a weaker intensity than was measured; the peaks at larger Q also follow this trend. The neutron results show this same shift relative to the predicted structure factor but the difference is less pronounced. To compare all our data, we display both $g(r)$ and $S(Q)$ from neutrons, x-rays, AIMD, and NNMD all vertically aligned in Fig. S1 of the Supplemental Material [66].

The partial structure factors in Figs. 4(b) and 5(b) help identify the contribution to the first $S(Q)$ peak as having Be—F, Be—Li, and Be—Be components. Using the partial-structure-factor results from simulations, we can evaluate the charge-alternation peaks described by Sharma *et al.* [98] The second peak at 2.7 $Å^{-1}$ appears to contain the charge alternations that are predicted to have positive correlations, with matching cation-cation and anion-anion pairs and negative correlations with opposite pairs. This peak is composed of positive F—F and Be—Be correlations along with negative F—Be correlations. Note that the negative ^{7}Li scattering length causes the F—Li and Be—Li correlation to be the opposite of the expected sign in the neutron structure factor.

IV. DISCUSSION

The coordination numbers of Be by fluorine, as calculated from the AIMD and NNMD simulations, are compared with the experimental values calculated from our neutron measurements in Table I. We find that these results agree to the nearest integer value, with the experimental values showing a slightly lower CN. Our CN calculations agree with other experimentally and computationally determined values [44,49,58,65]. A CN less than the nominal value of 4 is significant, since it indicates that Be is under-coordinated. A highly networked melt such as FLiBe with a capacity for under-coordination can be described as having an acid-base buffering capacity, which means that it maintains its fluoroacidity (the activity of F^-) upon the addition of solutes [44]. If the melt can accommodate the addition of solutes without a substantial change in its fluoroacidity, i.e., its structure as defined by association and dissociation reactions, it can solvate fission or corrosion products without major fluctuations in viscosity or other parameters affected by structure. An under-coordination of Be as indicated by our neutron experiments merits further analysis due to the relevance of the buffering capacity to macroscopic properties such as the viscosity and corrosivity.

As seen in Fig. 4(d), AIMD is able to accurately predict $S(Q)$ for $Q > 4$ $Å^{-1}$, corresponding to the local structure

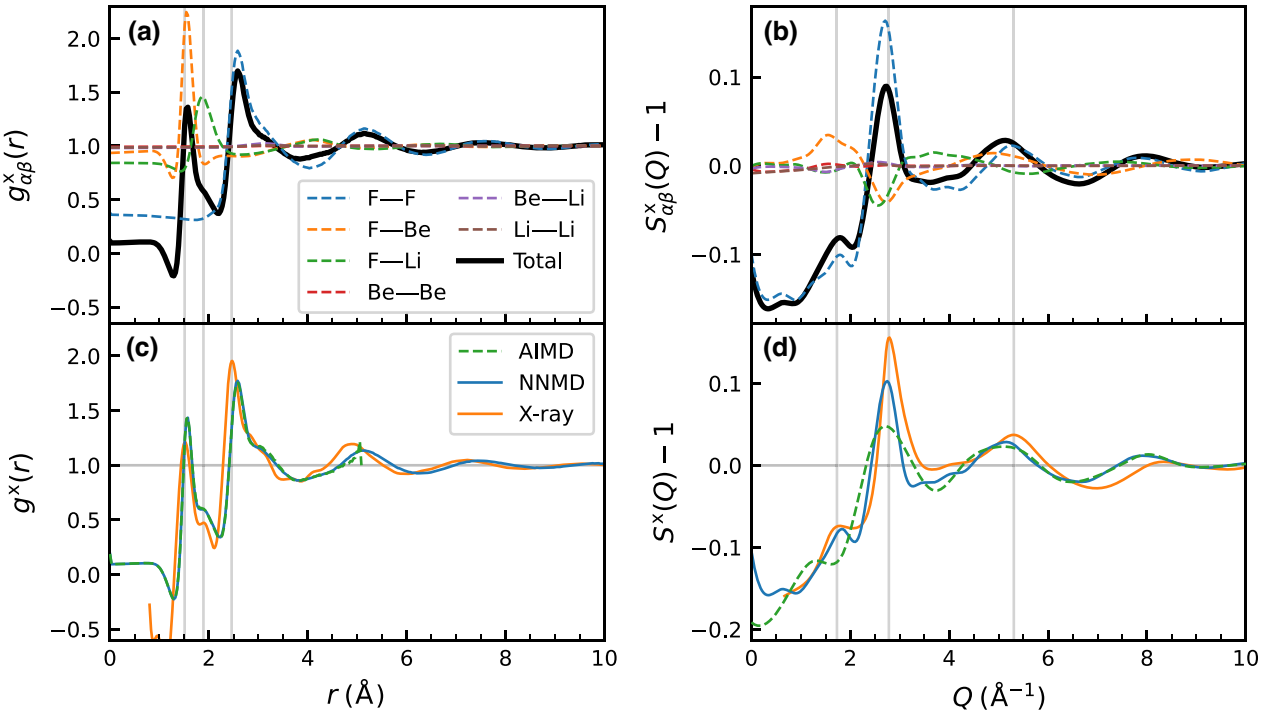

FIG. 5. The experimental and computational results of the x-ray scattering PDF and structure factor of FLiBe at 510 °C. (a),(b) The NNMD simulation results weighted with the atomic form factors, and (c),(d) x-ray scattering results with AIMD and NNMD simulation results for comparison.

within the first solvation shell. We evaluate the agreement of the AIMD-predicted structure factor with neutron measurements to be $R_\chi = 7.7\%$ for the neutron $S^n(Q)$. However, the AIMD-simulated spectra show significant differences in the peak heights and distances for $Q < 4$ Å^{-1}, showing inaccurate predictions of bond lengths and coordinations of intermediate-range structures. This is due to the small-cell limitations of the AIMD simulations, in which intermediate structures interact with their self-images across periodic boundary conditions. These limitations cause the AIMD simulations to produce artificial cutoffs on the intermediate-range structures, which are better represented in the NNMD simulations due to the larger cell sizes.

A better insight into this can be gained by quantitatively comparing the $([BeF_4]^{2-})_n$ cluster sizes between the AIMD and NNMD simulations. To identify the $([BeF_4]^{2-})_n$ clusters in the melt, the F—Be bond length was chosen to be 2.35 Å, which was obtained from the $r_{\min}$ value found in the F—Be partial PDF. The numbers of clusters of each size n were counted throughout the equilibrated NNMD and AIMD trajectories and were then normalized by the total number of Be atoms in each system. The distribution of cluster sizes larger than 2 is shown in Fig. 6(b). It was found that the occurrence of large $([BeF_4]^{2-})_n$ clusters (with $n \geq 4$) is less prominent in the AIMD simulations compared to NNMD, resulting in a greater mismatch in $S(Q)$ for $Q < 4$ Å^{-1} in Figs. 4(d) and 5(d). Meanwhile, as beryllium fluoride intermediate-range structures are better represented in large-cell NNMD simulations, the NNMD-predicted $S(Q)$ features (peak heights and positions) agree very well down to the lowest Q values with minor mismatches, with $R_\chi = 2.7\%$ for the neutron $S^n(Q)$.

The intermediate-range correlations in molten FLiBe in the form of $([BeF_4]^{2-})_n$ oligomers are evident through the first neutron-structure-factor peak at 1.7 Å^{-1}. An increase in correlations beyond the first shell (e.g., Be—Be) would cause a commensurate increase in the peak height and decrease in peak width, as shown in Figs. 4(d) and 5(d). Our NNMD simulations with a large cell size of approximately 21 Å and a simulation time of nearly 1.5 ns (compared to approximately 10.33 Å and 0.05 ns for AIMD) matched the experimental first peak both in intensity and width and, as such, sufficiently and accurately sampled the intermediate-range structures. The neutron-structure-factor measurements provide clear evidence for the intermediate-range structure in FLiBe. The x-ray structure is dominated by the fluoride ions with only small contributions from Be—F and Be—Be correlations. Having both neutron and x-ray measurements provides contrast in the contributions of each element to the respective structure factors. For example, the more pronounced differences between the x-ray and NNMD structure factors suggests

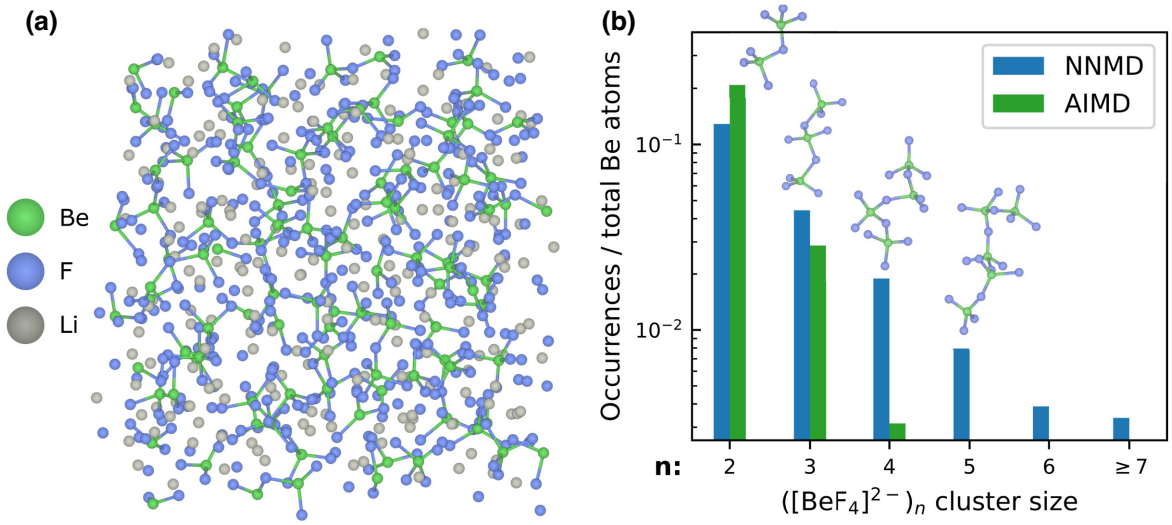

FIG. 6. (a) Snapshots of $([BeF_4]^{2-})_n$ clusters from FLiBe NNMD simulations at 700 °C with Li bonds removed from the visualization in the VESTA software package [97]. Note that the ions have been made all the same size for clarity. (b) The $([BeF_4]^{2-})_n$ cluster-size distribution normalized by the number of Be atoms, comparing AIMD and NNMD results. The snapshots of clusters with 2, 3, 4, and 5 Be cation centers are shown as a guide.

that the contribution of the fluorine atoms to the structure requires further refinements in modeling.

The disagreement between experiment and simulation could be caused by errors in predicting long-range interactions at the level of DFT and the interatomic potential fitting. To elaborate, the accumulated errors from approximations of semiempirical DFT–van der Waals (vdW) functionals in addition to the remaining contribution from long-range interactions could have led to the observed disagreement in peak positions and intensities between the simulated and measured neutron [Fig. 4(d)] and x-ray [Fig. 5(d)] structure factors, primarily at lower Q values. To address the former, a more thorough investigation is required in which the dispersion methods are systematically tested to more accurately account for the long-range interactions at the DFT level. For instance, we note from our study [99] that it is possible for compounding approximations of semiempirical DFT-vdW functionals to induce larger errors for the system, which are more strongly influenced by long-range interactions.

A further insight into the FLiBe structure as predicted in the AIMD and NNMD simulations can be gained by bond-angle-distribution analysis, as shown in Fig. 7. Both AIMD and NNMD predict an average F—Be—F angle of approximately 108 °, which corresponds to tetrahedral beryllium fluoride [Fig. 7(a)]. The peak in the Be—F—Be

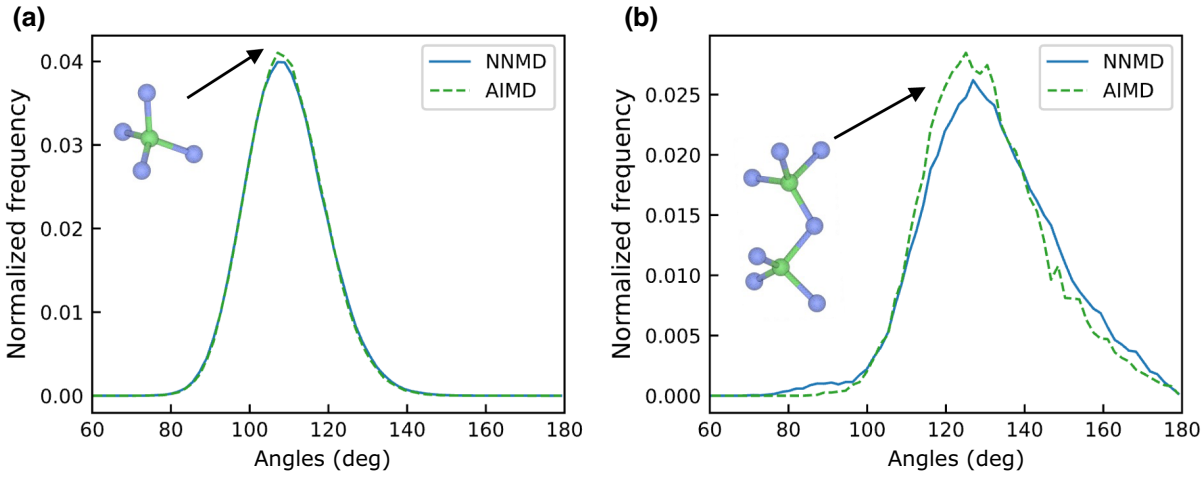

FIG. 7. The (a) F—Be—F and (b) Be—F—Be bond-angle distribution from molecular-dynamics simulations, normalized such that they integrate to one.

angle distribution [Fig. 7(b)] corresponds to corner-sharing beryllium fluoride complexes, which lead to extended-range ordering in the melt. Both the F—Be—F and the Be—F—Be angle-distribution plots are normalized such that their area integrates to one.

The demonstrated ability of NNIP to accurately predict intermediate-range structures and their populations despite being trained on small DFT simulation cells can be attributed to (1) training on a diverse range of configurations beyond a single AIMD trajectory and (2) sufficient charge screening of long-range interactions in FLiBe. First, training the NNIP on configurations sampled at both 510 °C and 700 °C enables accurate interpolation of atomic forces and energies over the wide range of NNMD-predicted configurations. Second, it is believed that the electrostatic potential beyond the 8-Å NNIP cutoff is sufficiently screened by polarizable solvent ions. This is consistent with our previous studies of other molten salts containing multivalent cations [59], in which the NNMD-predicted structures were supported by Raman spectroscopy. However, as mentioned previously, the compounding approximations of semiempirical DFT-vdW functionals and the NNIP truncation beyond 8 Å may induce larger errors for those systems and properties that are more strongly influenced by long-range interactions [99]. In such cases, other considerations may be required for the explicit treatment of these effects. Overall, here, the NNIP agrees with the scattering structure factor, providing confidence in the structural analysis.

V. CONCLUSIONS

In conclusion, we performed neutron and x-ray total-scattering measurements along with AIMD and NNMD simulations to characterize the structure of molten FLiBe. The combination of both neutron and x-ray measurements provides contrast in the contributions of each element to the structure of FLiBe. Moreover, the neutron first-structure-factor peak clearly presents the intermediate-range correlations comprised of $([BeF_4]^{2-})_n$ oligomers. The consistency between our experimental and computational findings provides confidence that this structural characterization may serve as a reference for future investigations of the fluoroberyllate melt structure and its properties. These results will prove useful in investigations of the influence of salt structure on its thermochemical and thermophysical properties, which are relevant for applications of molten salts. The use of salts in real energy systems requires the ability to calculate macroscopic properties such as conductivity and viscosity [43], salt acidity and corrosivity [44], solvation [45], and ion transport [59], which are strongly related to the intermediate-range structure beyond the NN. Therefore, our examination of the structure beyond the NN will have profound effects on the ability to predict how properties evolve in order to select optimal compositions. Specifically, our analysis of the oligomer structure and the CNs will be critical toward studying FLiBe salt in the presence of corrosion and fission products [44]. Overall, a broad and deep understanding of molten-salt structure, as enabled by varied high-resolution techniques, provides the basis for predicting the macroscopic properties relevant to engineering applications. We hope that this work will serve as a starting point for further studies of the effects of reactor salt compositions and conditions on salt structure and properties.

The experimental and computational data on the molten structure of FLiBe presented in this paper are openly available on Zenodo [100].

ACKNOWLEDGMENTS

This material is based upon work supported by the U.S. Department of Energy (DOE), Office of Nuclear Energy (NE), under Award No. 21-24563 (sample preparations, neutron, and x-ray measurements). We also acknowledge funding from the Los Alamos National Laboratory under subcontract 22206, through the Los Alamos National Laboratory Laboratory Directed Research and Development (LDRD) Project No. 20210113DR (neutron-diffraction data analysis), and the DOE-NE Nuclear Energy University Program (NEUP) under Award No. DE-NE0009204. A portion of this research used resources of the National Energy Research Scientific Computing Center, a DOE Office of Science User Facility supported by the Office of Science of the U.S. Department of Energy under Contract No. DE-AC02-05CH11231, using National Energy Research Scientific Computing Center (NERSC) Award No. BES-ERCAP0022445. A portion of this research used the 28-ID-1 beam line of the National Synchrotron Light Source II, a U.S. Department of Energy (DOE) Office of Science User Facility operated for the DOE Office of Science by Brookhaven National Laboratory under Contract No. DE-SC0012704. A portion of this research used resources at the Spallation Neutron Source, a DOE Office of Science User Facility operated by the Oak Ridge National Laboratory.

D.N.G., H.W., J.M., and R.C.G designed and prepared the neutron samples. G.Z., D.S., and B.K. designed and prepared the x-ray samples. S.F., D.N.G., and J.C.N. collected the neutron measurements. D.S. and D.O. collected the x-ray measurements. S.F. and J.C.N. analyzed the neutron measurements. S.F., D.S., J.C.N, and D.O. analyzed the x-ray measurements. R.C. and S.L. developed, conducted, and analyzed the results from the simulations. J.M., R.C.G., M.A., S.L., R.O.S., and B.K. conceptualized the project. S.L., R.O.S, and B.K. acquired funding. S.F., R.C., H.W., S.L, and B.K. wrote and edited the manuscript. All authors discussed the results and reviewed the manuscript.

Some of the authors currently have interests in, or relationships with, entities that are commercializing nuclear

technology. The content of this paper and the direction of the research presented herein has not been influenced by these entities, or by the authors' relationships with these entities.

[1] D. F. Williams and P. F. Britt, *Technology and Applied R&D Needs for Molten Salt Chemistry*, Technical Report (Oak Ridge National Laboratory (ORNL), Oak Ridge, Tennessee, 2017).

[2] P. N. Haubenreich and J. R. Engel, Experience with the molten-salt reactor experiment, Nucl. Appl. Technol. **8**, 118 (1970).

[3] H. G. MacPherson, The molten salt reactor adventure, Nucl. Sci. Eng. **90**, 374 (1985).

[4] L. Mathieu, D. Heuer, R. Brissot, C. Garzenne, C. Le Brun, D. Lecarpentier, E. Liatard, J. M. Loiseaux, O. Méplan, E. Merle-Lucotte, A. Nuttin, E. Walle, and J. Wilson, The thorium molten salt reactor: Moving on from the MSBR, Prog. Nucl. Energy **48**, 664 (2006).

[5] V. V. Ignatiev, O. S. Feynberg, A. V. Zagnitko, A. V. Merzlyakov, A. I. Surenkov, A. V. Panov, V. G. Subbotin, V. K. Afonichkin, V. A. Khokhlov, and M. V. Kormilitsyn, Molten-salt reactors: New possibilities, problems and solutions, At. Energy **112**, 157 (2012).

[6] C. Andreades, A. T. Cisneros, J. K. Choi, A. Y. K. Chong, M. Fratoni, S. Hong, L. R. Huddar, K. D. Huff, J. Kendrick, D. L. Krumwiede, M. R. Laufer, M. Munk, R. O. Scarlat, and N. Zweibau, Design summary of the Mark-I pebble-bed, fluoride salt–cooled, high-temperature reactor commercial power plant, Nucl. Technol. **195**, 223 (2016).

[7] B. N. Sorbom, J. Ball, T. R. Palmer, F. J. Mangiarotti, J. M. Sierchio, P. Bonoli, C. Kasten, D. A. Sutherland, H. S. Barnard, C. B. Haakonsen, J. Goh, C. Sung, and D. G. Whyte, ARC: A compact, high-field, fusion nuclear science facility and demonstration power plant with demountable magnets, Fusion Eng. Des. **100**, 378 (2015).

[8] C. Forsberg, G. Zheng, R. G. Ballinger, and S. T. Lam, Fusion blankets and fluoride-salt-cooled high-temperature reactors with FLiBe salt coolant: Common challenges, tritium control, and opportunities for synergistic development strategies between fission, fusion, and solar salt technologies, Nucl. Technol. **206**, 1778 (2020).

[9] C. W. Forsberg, Market basis for salt-cooled reactors: Dispatchable heat, hydrogen, and electricity with assured peak power capacity, Nucl. Technol. **206**, 1659 (2020).

[10] B. Mignacca and G. Locatelli, Economics and finance of molten salt reactors, Prog. Nucl. Energy **129**, 103503 (2020).

[11] R. W. Moir, Recommendations for a restart of molten salt reactor development, Energy Conversion and Management ICENES'2007, 13th International Conference on Emerging Nuclear Energy Systems, June 3–8, 2007, İstanbul, Turkiye **49**, 1849 (2008).

[12] B. M. Elsheikh, Safety assessment of molten salt reactors in comparison with light water reactors, J. Radiat. Res. Appl. Sci. **6**, 63 (2013).

[13] D. F. Williams and K. T. Clarno, Evaluation of salt coolants for reactor applications, Nucl. Technol. **163**, 330 (2008).

[14] V. Khokhlov, V. Ignatiev, and V. Afonichkin, Evaluating physical properties of molten salt reactor fluoride mixtures, J. Fluorine Chem. Fluorine Nucl. Energy **130**, 30 (2009).

[15] Sylvie. Delpech, C. Cabet, C. Slim, and G. S. Picard, Molten fluorides for nuclear applications, Mater. Today **13**, 34 (2010).

[16] W. R. Grimes, Molten-salt reactor chemistry, Nucl. Appl. Technol. **8**, 137 (1970).

[17] M. S. Sohal, M. A. Ebner, P. Sabharwall, and P. Sharpe, *Engineering Database of Liquid Salt Thermophysical and Thermochemical Properties*, Technical Report INL/EXT-10-18297 (Idaho National Laboratory (INL), Idaho Falls, Idaho, 2010).

[18] S. Cantor, W. T. Ward, and C. T. Moynihan, Viscosity and density in molten BeF_2-LiF solutions, J. Chem. Phys. **50**, 2874 (1969).

[19] O. Yu. Tkacheva, A. V. Rudenko, A. A. Kataev, P. N. Mushnikov, A. S. Kholkina, and Yu. P. Zaikov, The viscosity of molten salts based on the LiF-BeF_2 system, Russ. J. Non-Ferrous Metals **63**, 276 (2022).

[20] K. Yajima, H. Moriyama, J. Oishi, and Y. Tominaga, Surface tension of lithium fluoride and beryllium fluoride binary melt, J. Phys. Chem. **86**, 4193 (1982).

[21] T. Lichtenstein, M. A. Rose, J. Krueger, E. Wu, and M. A. Williamson, Thermochemical property measurements of FLiNaK and FLiBe in FY 2020, 34 (2020).

[22] E. Il'ina, P. Mushnikov, S. Pershina, A. Rudenko, A. Redkin, Yu. Zaikov, A. Kholkina, and V. Voronin, Thermal properties of LiF-BeF_2 and LiF-BeF_2-UF_4 systems as applied to molten salt reactor technologies, J. Mol. Liq. **344**, 117731 (2021).

[23] R. Vidrio, S. Mastromarino, E. Still, L. Chapdelaine, and R. O. Scarlat, Density and thermal expansivity of molten 2LiF-BeF_2 (FLiBe): Measurements and uncertainty quantification, J. Chem. Eng. Data **67**, 3517 (2022).

[24] D. R. Olander, G. T. Fukuda, and C. F. Baes, Equilibrium pressures over BeF_2/LiF(FLiBe) molten mixtures, Fusion Sci. Technol. **41**, 141 (2002).

[25] M. R. Zaghloul, D. K. Sze, and A. R. Raffray, Thermophysical properties and equilibrium vapor-composition of lithium fluoride-beryllium fluoride (2LiF/BeF_2) molten salt, Fusion Sci. Technol. **44**, 344 (2003).

[26] S. Fukada and A. Nakamura, Estimation of melting points for some binary and tertiary fluoride molten salts, Fusion Sci. Technol. **66**, 322 (2014).

[27] B. F. Hitch and C. F. J. Baes, Electromotive force study of molten lithium fluoride–beryllium fluoride solutions, Inorg. Chem. **8**, 201 (1969).

[28] K. A. Romberger and J. Braunstein, Transference numbers and mobilities in molten mixtures of beryllium fluoride and lithium fluoride, Inorg. Chem. **9**, 1273 (1970).

[29] K. A. Romberger, J. Braustein, and R. E. Thoma, New electrochemical measurements of the liquidus in the lithium fluoride–beryllium fluoride system: Congruency of lithium beryllium fluoride (Li_2BeF_4), J. Phys. Chem. **76**, 1154 (1972).

[30] K. Igarashi, Y. Okamoto, J. Mochinaga, and H. Ohno, X-ray diffraction study of molten eutectic LiF-NaF-KF mixture, J. Chem. Soc., Faraday Trans. 1 **84**, 4407 (1988).

[31] B. A. Frandsen, S. D. Nickerson, A. D. Clark, A. Solano, R. Baral, J. Williams, J. Neuefeind, and M. Memmott, The structure of molten FLiNaK, J. Nucl. Mater. **537**, 152219 (2020).

[32] Q.-J. Li, D. Sprouster, G. Zheng, J. C. Neuefeind, A. D. Braatz, J. Mcfarlane, D. Olds, S. Lam, J. Li, and B. Khaykovich, Complex structure of molten NaCl-$CrCl_3$ salt: Cr-Cl octahedral network and intermediate-range order, ACS Appl. Energy Mater. **4**, 3044 (2021).

[33] D. Sprouster, G. Zheng, S.-C. Lee, D. Olds, C. Agca, J. McFarlane, Y. Z, and B. Khaykovich, Molecular structure and phase equilibria of molten fluoride salt with and without dissolved cesium: FLiNaK-CsF (5 mol %), ACS Appl. Energy Mater. **5**, 8067 (2022).

[34] M. Kondo, T. Nagasaka, A. Sagara, N. Noda, T. Muroga, Q. Xu, M. Nagura, A. Suzuki, and T. Terai, Metallurgical study on corrosion of austenitic steels in molten salt LiF-BeF_2 (FLiBe), J. Nucl. Mater. Fusion Reactor Mater. **386–388**, 685 (2009).

[35] L. C. Olson, J. W. Ambrosek, K. Sridharan, M. H. Anderson, and T. R. Allen, Materials corrosion in molten LiF-NaF-KF salt, J. Fluorine Chem. Fluorine Nucl. Energy **130**, 67 (2009).

[36] G. Zheng, B. Kelleher, G. Cao, M. Anderson, T. Allen, and K. Sridharan, Corrosion of 316 stainless steel in high temperature molten Li_2BeF_4 (FLiBe) salt, J. Nucl. Mater. **461**, 143 (2015).

[37] S. Guo, J. Zhang, W. Wu, and W. Zhou, Corrosion in the molten fluoride and chloride salts and materials development for nuclear applications, Prog. Mater. Sci. **97**, 448 (2018).

[38] J. Zhang, C. W. Forsberg, M. F. Simpson, S. Guo, S. T. Lam, R. O. Scarlat, F. Carotti, K. J. Chan, P. M. Singh, W. Doniger, K. Sridharan, and J. R. Keiser, Redox potential control in molten salt systems for corrosion mitigation, Corros. Sci. **144**, 44 (2018).

[39] S. Fayfar, G. Zheng, D. Sprouster, M. S. J. Marshall, E. Stavitski, D. Leshchev, and B. Khaykovich, In-situ analysis of corrosion products in molten salt: X-ray absorption reveals both ionic and metallic species, ACS Omega **8**, 24673 (2023).

[40] M. Salanne, C. Simon, P. Turq, R. J. Heaton, and P. A. Madden, A first-principles description of liquid BeF_2 and its mixtures with LiF: 2. Network formation in LiF-BeF_2, J. Phys. Chem. B **110**, 11461 (2006).

[41] T. Porter, M. M. Vaka, P. Steenblik, and D. Della Corte, Computational methods to simulate molten salt thermophysical properties, Commun. Chem. **5**, 1 (2022).

[42] A. L. Smith, E. Capelli, R. J. M. Konings, and A. E. Gheribi, A new approach for coupled modelling of the structural and thermo-physical properties of molten salts. Case of a polymeric liquid LiF-BeF_2, J. Mol. Liq. **299**, 112165 (2020).

[43] M. Salanne, C. Simon, P. Turq, and P. A. Madden, Conductivity-viscosity-structure: Unpicking the relationship in an ionic liquid, J. Phys. Chem. B **111**, 4678 (2007).

[44] N. Winner, H. Williams, R. O. Scarlat, and M. Asta, Ab-initio simulation studies of chromium solvation in molten fluoride salts, J. Mol. Liq. **335**, 116351 (2021).

[45] S. Lam, Q.-J. Li, J. Mailoa, C. Forsberg, R. Ballinger, and J. Li, The impact of hydrogen valence on its bonding and transport in molten fluoride salts, J. Mater. Chem. A **9**, 1784 (2021).

[46] B. L. Tremillon, in *Molten Salt Chemistry: An Introduction and Selected Applications*, NATO ASI Series, edited by G. Mamantov and R. Marassi (Springer Netherlands, Dordrecht, 1987), p. 279.

[47] P. Chamelot and J. C. Poignet, in *Sels Fondus à Haute Température*, edited by P. Taxil (Presses polytechniques et universitaires romandes, Lausanne, 2009).

[48] D. F. Williams, *Assessment of Candidate Molten Salt Coolants for the NGNP/NHI Heat-Transfer Loop*, Technical Report ORNL/TM-2006/69 (Oak Ridge National Laboratory (ORNL), Oak Ridge, Tennessee, 2006).

[49] F. Vaslow and A. H. Narten, Diffraction pattern and structure of molten BeF_2-LiF solutions, J. Chem. Phys. **59**, 4955 (1973).

[50] C. F. Baes, A polymer model for BeF_2 and SiO_2 melts, J. Solid State Chem. **1**, 159 (1970).

[51] A. Rahman, R. H. Fowler, and A. H. Narten, Structure and motion in liquid BeF_2, $LiBeF_3$, and LiF from molecular dynamics calculations, J. Chem. Phys. **57**, 3010 (1972).

[52] G. E. Moore, *Chemistry Division Annual Progress Report for Period Ending May 20, 1974*, Technical Report ORNL-4706 (Oak Ridge National Laboratory (ORNL), Oak Ridge, Tennessee, 1974).

[53] A. S. Quist, J. B. Bates, and G. E. Boyd, Raman spectra of tetrafluoroberyllate ion in molten sodium fluoride and lithium fluoride to 686.deg., J. Phys. Chem. **76**, 78 (1972).

[54] L. M. Toth, J. B. Bates, and G. E. Boyd, Raman spectra of $Be_2F_7^{3-}$ and higher polymers of beryllium fluorides in the crystalline and molten state, J. Phys. Chem. **77**, 216 (1973).

[55] J. Dai, H. Han, Q. Li, and P. Huai, First-principle investigation of the structure and vibrational spectra of the local structures in LiF-BeF_2 molten salts, J. Mol. Liq. **213**, 17 (2016).

[56] Y. Li, X. Liu, B. Wang, and C. Wang, Raman and theoretical studies on structural evolution of Li−2BeF_4 and binary LiF-BeF_2 melts, J. Mol. Liq. **325**, 115208 (2021).

[57] K. Baral, S. San, R. Sakidja, A. Couet, K. Sridharan, and W.-Y. Ching, Temperature-dependent properties of molten Li_2BeF_4 salt using *ab initio* molecular dynamics, ACS Omega **6**, 19822 (2021).

[58] S. Attarian, D. Morgan, and I. Szlufarska, Thermophysical properties of FLiBe using moment tensor potentials, J. Mol. Liq. **368**, 120803 (2022).

[59] R. Chahal, S. Roy, M. Brehm, S. Banerjee, V. Bryantsev, and S. T. Lam, Transferable deep learning potential reveals intermediate-range ordering effects in LiF-NaF-ZrF4 molten salt, JACS Au **2**, 2693 (2022).

[60] J. Behler and M. Parrinello, Generalized neural-network representation of high-dimensional potential-energy surfaces, Phys. Rev. Lett. **98**, 146401 (2007).

[61] L. Zhang, J. Han, H. Wang, R. Car, and W. E, Deep potential molecular dynamics: A scalable model with the

accuracy of quantum mechanics, Phys. Rev. Lett. **120**, 143001 (2018).
[62] A. Rodriguez, S. Lam, and M. Hu, Thermodynamic and transport properties of LiF and FLiBe molten salts with deep learning potentials (2021).
[63] S. T. Lam, Q.-J. Li, R. Ballinger, C. Forsberg, and J. Li, Modeling LiF and FLiBe molten salts with robust neural network interatomic potential, ACS Appl. Mater. Interfaces **13**, 24582 (2021).
[64] S.-C. Lee, Y. Zhai, Z. Li, N. P. Walter, M. Rose, B. J. Heuser, and Y. Z, Comparative studies of the structural and transport properties of molten salt FLiNaK using the machine-learned neural network and reparametrized classical forcefields, J. Phys. Chem. B **125**, 10562 (2021).
[65] H. Wang, B. Yue, L. Yan, T. Jiang, and S. Peng, First-principles molecular dynamics study of the behavior of tritium in molten LiF-BeF_2 eutectic, J. Mol. Liq. **345**, 117027 (2022).
[66] See the Supplemental Material at http://link.aps.org/supplemental/10.1103/PRXEnergy.3.013001 for all results plotted together and vertically aligned; all calculated goodness-of-fit statistical values using Eq. (6); comparison of the MD results with Refs. [44,58]; MD results varying the Li-enrichment concentration; raw neutron data and a description of the filtering process; details about the MD cutoff radius; x-ray measurements before background subtractions and standard measurements; details on the methods to calculate the first-peak distances and CN-fitting procedures; neutron $S(Q)$ peak fitting versus temperature; and MD results at both temperatures compared.
[67] J. Neuefeind, M. Feygenson, J. Carruth, R. Hoffmann, and K. K. Chipley, The Nanoscale Ordered MAterials Diffractometer NOMAD at the Spallation Neutron Source SNS, Nucl. Instrum. Methods Phys. Res., Sect. B **287**, 68 (2012).
[68] M. T. McDonnell, D. P. Olds, K. L. Page, J. C. Neufeind, M. G. Tucker, J. C. Bilheux, W. Zhou, and P. F. Peterson, ADDIE: ADvanced DIffraction Environment—a software environment for analyzing neutron diffraction data, Acta Crystallogr., Sect. A: Found. Adv. **73**, a377 (2017).
[69] O. Ivashkevych, M. Abeykoon, J. Adams, G. Bischof, E. Dooryhee, J. Li, R. Petkus, J. Trunk, and Z. Yin, in *17th International Conference on Accelerator and Large Experimental Physics Control Systems (ICALEPCS'19), New York, 05-11 October 2019* (JACOW Publishing, Geneva, Switzerland, 2020), p. 1584.
[70] J. Kieffer and D. Karkoulis, PyFAI, a versatile library for azimuthal regrouping, J. Phys.: Conf. Ser. **425**, 202012 (2013).
[71] P. Juhás, T. Davis, C. L. Farrow, and S. J. L. Billinge, PDFgetX3: A rapid and highly automatable program for processing powder diffraction data into total scattering pair distribution functions, J. Appl. Crystallogr. **46**, 560 (2013).
[72] P. J. Brown, A. G. Fox, E. N. Maslen, M. A. O'Keefe, and B. T. M. Willis, in *International Tables for Crystallography*, Vol. C, edited by H. Fuess, Th. Hahn, H. Wondratschek, U. Müller, U. Shmueli, E. Prince, A. Authier, V. Kopský, D. B. Litvin, M. G. Rossmann, E. Arnold, S. Hall, B. McMahon, and E. Prince (International Union of Crystallography, Chester, England, 2006) 1st ed., p. 554.
[73] J. Neuefeind, High energy XRD investigations of liquids, J. Mol. Liq. Mol. Struct. Dyn. Liq. **98–99**, 87 (2002).
[74] H. E. Fischer, A. C. Barnes, and P. S. Salmon, Neutron and x-ray diffraction studies of liquids and glasses, Rep. Prog. Phys. **69**, 233 (2006).
[75] P. F. Peterson, D. Olds, M. T. McDonnell, and K. Page, Illustrated formalisms for total scattering data: A guide for new practitioners, J. Appl. Crystallogr. **54**, 317 (2021).
[76] K. Zhou and B. Liu, *Molecular Dynamics Simulation: Fundamentals and Applications* (Elsevier, Amsterdam, 2022).
[77] A. K. Soper, *GudrunN and GudrunX: Programs for correcting raw neutron and x-ray diffraction data to differential scattering cross section* (Science & Technology Facilities Council, Swindon, United Kingdom, 2011).
[78] P. B. Lond, P. S. Salmon, and D. C. Champeney, Structure of nickel(2+) solutions in ethylene glycol by neutron diffraction: An observed hydrogen bond between the solvent ligands in the first and second cation coordination shells, J. Am. Chem. Soc. **113**, 6420 (1991).
[79] A. C. Hannon and J. M. Parker, The structure of aluminate glasses by neutron diffraction, J. Non-Cryst. Solids Phys. Non-Cryst. Solids 9 **274**, 102 (2000).
[80] L. Hennet, J. W. E. Drewitt, D. R. Neuville, V. Cristiglio, J. Kozaily, S. Brassamin, D. Zanghi, and H. E. Fischer, Neutron diffraction of calcium aluminosilicate glasses and melts, J. Non-Cryst. Solids Struct., Dyn. Appl. Non-Cryst. Solids Disordered Mater. **451**, 89 (2016).
[81] G. J. Janz, G. L. Gardner, U. Krebs, and R. P. T. Tomkins, Molten salts: Volume 4, Part 1, Fluorides and mixtures electrical conductance, density, viscosity, and surface tension data, J. Phys. Chem. Ref. Data **3**, 1 (1974).
[82] G. Kresse and J. Furthmüller, Efficient iterative schemes for *ab initio* total-energy calculations using a plane-wave basis set, Phys. Rev. B **54**, 11169 (1996).
[83] J. P. Perdew, K. Burke, and M. Ernzerhof, Generalized gradient approximation made simple, Phys. Rev. Lett. **77**, 3865 (1996).
[84] S. Grimme, J. Antony, S. Ehrlich, and H. Krieg, A consistent and accurate ab initio parametrization of density functional dispersion correction (DFT-D) for the 94 elements H-Pu, J. Chem. Phys. **132**, 154104 (2010).
[85] H. O. Nam, A. Bengtson, K. Vörtler, S. Saha, R. Sakidja, and D. Morgan, First-principles molecular dynamics modeling of the molten fluoride salt with Cr solute, J. Nucl. Mater. **449**, 148 (2014).
[86] L. Martínez, R. Andrade, E. G. Birgin, and J. M. Martínez, PACKMOL: A package for building initial configurations for molecular dynamics simulations, J. Comput. Chem. **30**, 2157 (2009).
[87] R. Chahal, S. Banerjee, and S. T. Lam, Short- to intermediate-range structure, transport, and thermophysical properties of LiF-NaF-ZrF_4 molten salts, Front. Phys. **10**, 830468 (2022).
[88] H. Wang, L. Zhang, J. Han, and W. E, DeePMD-kit: A deep learning package for many-body potential energy representation and molecular dynamics, Comput. Phys. Commun. **228**, 178 (2018).

[89] L. Zhang, J. Han, H. Wang, W. Saidi, R. Car, and W. E, in *Advances in Neural Information Processing Systems*, Vol. 31 (Curran Associates, Inc., Montreal, 2018).
[90] S. Plimpton, Fast parallel algorithms for short-range molecular dynamics, J. Comput. Phys. **117**, 1 (1995).
[91] W. G. Hoover, Canonical dynamics: Equilibrium phase-space distributions, Phys. Rev. A **31**, 1695 (1985).
[92] A. C. Wright, Neutron scattering from vitreous silica. V. The structure of vitreous silica: What have we learned from 60 years of diffraction studies?, J. Non-Cryst. Solids Proceedings of the First PAC RIM Meeting on Glass and Optical Materials **179**, 84 (1994).
[93] J. Du, C. J. Benmore, R. Corrales, R. T. Hart, and J. K. R. Weber, A molecular dynamics simulation interpretation of neutron and x-ray diffraction measurements on single phase Y_2O_3-Al_2O_3 glasses, J. Phys.: Condens. Matter **21**, 205102 (2009).
[94] O. L. G. Alderman, G. Ferlat, A. Baroni, M. Salanne, M. Micoulaut, C. J. Benmore, A. Lin, A. Tamalonis, and J. K. R. Weber, Liquid B_2O_3 up to 1700 K: X-ray diffraction and boroxol ring dissolution, J. Phys.: Condens. Matter **27**, 455104 (2015).
[95] M. Wilson, Structure and dynamics in network-forming materials, J. Phys.: Condens. Matter **28**, 503001 (2016).
[96] Q. Zhou, Y. Shi, B. Deng, J. Neuefeind, and M. Bauchy, Experimental method to quantify the ring size distribution in silicate glasses and simulation validation thereof, Sci. Adv. **7**, eabh1761 (2021).
[97] K. Momma and F. Izumi, VESTA 3 for three-dimensional visualization of crystal, volumetric and morphology data, J. Appl. Crystallogr. **44**, 1272 (2011).
[98] S. Sharma, A. S. Ivanov, and C. J. Margulis, A brief guide to the structure of high-temperature molten salts and key aspects making them different from their low-temperature relatives, the ionic liquids, J. Phys. Chem. B **125**, 6359 (2021).
[99] S. Lam, S. Banerjee, and R. Chahal, in *Transactions of the American Nuclear Society*, Vol. 126 (Transactions of the American Nuclear Society, Anaheim, 2022), p. 385.
[100] https://doi.org/10.5281/zenodo.7992414